# Virtual Image Correlation uncertainty

**M. L. M. François**

**Abstract** The Virtual Image Correlation method applies for the measurement of silhouettes boundaries with sub-pixel precision. It consists in a correlation between the image of interest and a virtual image based on a parametrized curve. Thanks to a new formulation, it is shown that the method is exact in 1D, insensitive to local curvature and to contrast variation, and that the bias induced by luminance variation can be easily corrected. Optimal value of the virtual image width, the sole parameter of the method, and optimal numerical settings are established. An estimator is proposed to assess the relevance of the user-chosen curve to describe the contour with a sub-pixel precision. Analytical formulas are given for the measurement uncertainty in both cases of noiseless and noisy images and their prediction is successfully compared to numerical tests.

**Keywords** Virtual Image Correlation · Digital Image Correlation

## 1 Introduction

The Virtual Image Correlation (VIC) originates from the global form of the Digital Image Correlation (DIC) method [7,8]. However, in the VIC, the second image is an elementary and unitary virtual one which mimics the white to black gradient of the boundary and whose shape is defined from a parametrized curve. At convergence, when virtual and physical images are close as possible, the curve shape represents a measurement of the contour.

Marc Louis Maurice François
GeM, UMR 6183, CNRS-Université de Nantes — École Centrale Nantes, 2, rue de la Houssinière BP 92208, 44322 Nantes Cedex 3, France
Tel.: +33-2-51125521
E-mail: marc.francois@univ-nantes.fr

The very first version of the VIC was dedicated to open contour measurement [6]. Its extension to silhouette measurement followed [15,12] then a numerically efficient version benefitting of close DIC developments [13]. Further work concerned various application of the method for the mechanical testings [5,2,4] or in medicine [9]. The major interest of the VIC is its precision, in some case better than $10^{-3}$ pixels [15]. However, the present article was motivated by a need for more objective evaluation of the uncertainty, with predictive formulas.

In Sec. 2 is shown a slightly modified version of the method, in which the mean square distance between virtual and physical images is calculated in the frame of the virtual image. This gives both a slightly better precision and much simpler equations.

Section 3 is dedicated to the quantification of uncertainties. It begins by establishing a set of simplified equations, which are used at first to prove that the method is theoretically exact in 1D. The VIC requires the chosen curve family to be able to fit the contour of interest. Aiming sub-pixel precision, the simple observation of the obtained curve superposed to the silhouette is not sufficient to check this point. A signed distance is proposed, which consists in a local measurement of the silhouette in the virtual image frame. Its graph emphasis the local accuracy of the identification and its spectral analysis informs about the relevance of the chosen curve to depict the contour. The image discretization is an inevitable cause of uncertainty that leads to the ultimate accuracy of the method. An empirical law, deducted from statistics on numerical tests, is proposed to assess it. Effect of imperfect brightness and contrast are studied analytically. It is shown that contrast has no effect on the precision but that brightness induces a bias which can be suppressed by a linear correction of the image. Then, the measurement uncertainty due to image noise is quantified by a simple analytical formula. A simple graph summarizes the expected accuracy as a function of the image noise and the number of parameters of the curve.

Section 4 validates the proposed expressions of uncertainties, through statistics on old [15] and new synthetic tests. In addition to the comparisons already made (in [15]) with the Fast Marching Algorithm [16] and the Steger's method [17], new comparisons are made here with the active contour method [10] and the recent method of Trujilo-Pino [21] which are both known for their sub-pixel precision. Tests on noisy images also emphasize the robustness of the VIC. For all synthetic images used in this article, the grey levels of the transition pixels (through which the edge passes) are calculated from the ratio of the white (background) and black (silhouette) surfaces seen by the pixel.
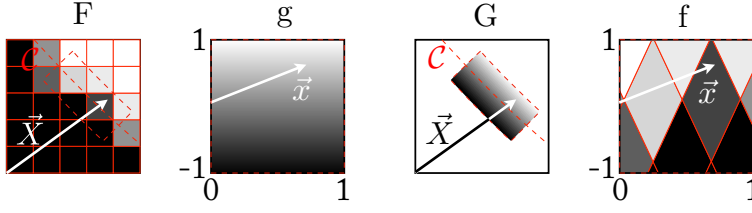
**Fig. 1** Sketch of the VIC method

## 2 The VIC method

The silhouette of interest in image F is measured by finding the best coincidence between F and a virtual image G based on a parametrized curve $\mathcal{C}$ (see Fig. 1). Image F has grey levels $F(\mathbf{X})$ where $\mathbf{X}$ is the position vector of components $(X_1, X_2)$ associated to the pixel frame. The virtual image G of gray levels $G(\mathbf{X})$ is a deformation of an elementary image g of grey levels $g(\mathbf{x})$ such as:

$$G(\mathbf{X}) = g(\mathbf{x}) \tag{1}$$

$$g(\mathbf{x}) = \frac{1 + x_2}{2} \tag{2}$$

where the position vector $\mathbf{x}$ has components $x_1 \in [0, 1]$ and $x_2 \in [-1, 1]$. The linear evolution of the gray level $g(\mathbf{x})$ is chosen in order G to be roughly similar to the gray level evolution across the boundary in F. A current point $\mathbf{X}$ of G is defined from the user-chosen parametric curve $\mathcal{C}$ of current point $\mathbf{X}^c$ (see Fig. 2):

$$\mathbf{X}(x_1, x_2, \lambda_p) = \mathbf{X}^c(x_1, \lambda_p) + R x_2\, \mathbf{e}_r(x_1, \lambda_p), \tag{3}$$

where $x_1$ is used as the curve parameter, the $\lambda_p$ are the (researched) shape pa-
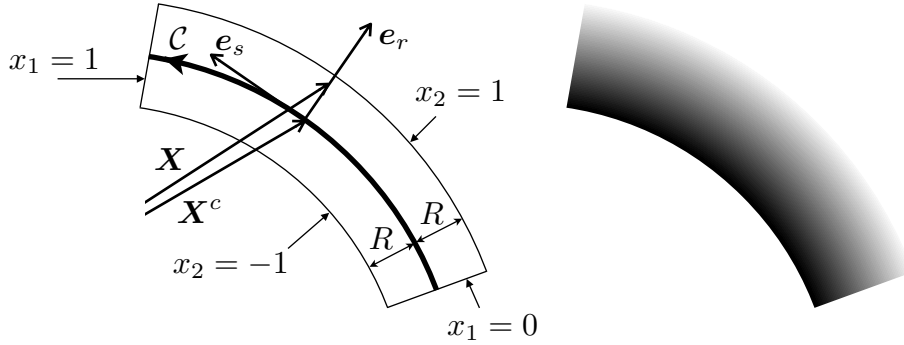


**Fig. 2** Virtual image geometry (left) and grey levels (right)

rameters and $(\mathbf{e}_s, \mathbf{e}_r)$ are respectively the unitary tangent and normal vectors

to the curve:

$$\mathbf{e}_s = \frac{\partial \mathbf{X}^c}{\partial x_1} \left\| \frac{\partial \mathbf{X}^c}{\partial x_1} \right\|^{-1} \tag{4}$$

$$\mathbf{e}_r = \mathbf{e}_s \times \mathbf{e}_z \tag{5}$$

where $\times$ denotes the cross product and $\mathbf{e}_z$ is the unitary vector normal to the plane. Above definition guarantees that $\mathbf{e}_r$ points uniformly outside any closed curve orientated positively.

The goal of the method is to find the shape parameters $\lambda_p$ of $\mathcal{C}$ for which F and G are in best coincidence. As for some DIC methods [7], the mean square difference between the two images is minimized:

$$\Psi = \frac{\int \int (F(\mathbf{X}) - G(\mathbf{X}))^2 dX_1 dX_2}{\int \int dX_1 dX_2} \tag{6}$$

This expression was used in the very first version of the VIC [6,15] in which the surface area $2RL$ (the denominator) was constant. Neglecting the surface variation allows the use of numerically efficient DIC algorithms [13] but with a loss of accuracy. Strictly speaking, the length $L$ of the curve, so the area, is not constant. Furthermore, the differential surface element $dX_1 dX_2$ depends, by Eq. (38), upon the curvature and neglecting it creates a slight but unwanted line tension effect. The proposed minimization function is expressed in the frame of the virtual image:

$$\psi = \frac{\int \int (f(\mathbf{x}) - g(\mathbf{x}))^2 dx_1 dx_2}{\int \int dx_1 dx_2}, \tag{7}$$

in which $f(\mathbf{x}) = F(\mathbf{X})$. The denominator represents the constant surface area of g (of value 2) and the differential surface element $dx_1 dx_2$ is independent of the curvature. The minimization of $\Psi$ with respect to $\lambda_p$ is achieved by using a Newton scheme, solving iteratively the $N \times N$ linear system:

$$\frac{\partial^2 \psi}{\partial \lambda_p \partial \lambda_q} \Delta \lambda_q = -\frac{\partial \psi}{\partial \lambda_p} \tag{8}$$

where $\Delta \lambda_q$ is the corrector of the current values of the $N$ curve parameters $\lambda_q$ and where:

$$2\psi(\lambda_p) = \int_{-1}^{1} \int_{0}^{1} \left( F(\mathbf{X}(x_1, x_2, \lambda_p)) - g(x_2) \right)^2 dx_1 dx_2 \tag{9}$$

$$\frac{\partial \psi}{\partial \lambda_p} = \int_{-1}^{1} \int_{0}^{1} \left( \frac{\partial F}{\partial \mathbf{X}} \cdot \frac{\partial \mathbf{X}}{\partial \lambda_p} \right) (f - g) dx_1 dx_2 \tag{10}$$

$$\frac{\partial^2 \psi}{\partial \lambda_p \partial \lambda_q} = \int_{-1}^{1} \int_{0}^{1} \left[ \left( \frac{\partial \mathbf{X}}{\partial \lambda_p} \cdot \frac{\partial^2 F}{\partial \mathbf{X}^2} \cdot \frac{\partial \mathbf{X}}{\partial \lambda_q} + \frac{\partial F}{\partial \mathbf{X}} \cdot \frac{\partial^2 \mathbf{X}}{\partial \lambda_p \partial \lambda_q} \right) (f - g) + \right.$$
$$\left. \left( \frac{\partial F}{\partial \mathbf{X}} \cdot \frac{\partial \mathbf{X}}{\partial \lambda_p} \right) \left( \frac{\partial F}{\partial \mathbf{X}} \cdot \frac{\partial \mathbf{X}}{\partial \lambda_q} \right) \right] dx_1 dx_2 \tag{11}$$

Annex A shows that it is possible, under some reasonable assumptions, to take into account only the last term (as done in DIC [7]) thus:

$$\frac{\partial^2 \psi}{\partial \lambda_p \partial \lambda_q} \simeq \int_{-1}^{1} \int_{0}^{1} \left( \frac{\partial F}{\partial \mathbf{X}} \cdot \frac{\partial \mathbf{X}}{\partial \lambda_p} \right) \left( \frac{\partial F}{\partial \mathbf{X}} \cdot \frac{\partial \mathbf{X}}{\partial \lambda_q} \right) dx_1 dx_2 \qquad (12)$$

in which, from Eq. (3):

$$\frac{\partial \mathbf{X}}{\partial \lambda_p} = \frac{\partial \mathbf{X}^c}{\partial \lambda_p} - R x_2 \left\| \frac{\partial \mathbf{X}^c}{\partial x_1} \right\|^{-1} \left( \frac{\partial^2 \mathbf{X}^c}{\partial \lambda_p \partial x_1} \cdot \mathbf{e}_r \right) \mathbf{e}_s \qquad (13)$$

The derivatives of the curve points $\mathbf{X}^c$ are supposed either analytically or numerically known. Curvilinear abscissa $s$ and curvature $\rho$ are:

$$s = \int_{0}^{x_1} \left\| \frac{\partial \mathbf{X}^c}{\partial \xi_1} \right\| d\xi_1 \qquad (14)$$

$$\rho = - \left( \frac{\partial^2 \mathbf{X}^c}{\partial x_1^2} \cdot \mathbf{e}_r \right) \left\| \frac{\partial \mathbf{X}^c}{\partial x_1} \right\|^{-2} \qquad (15)$$

and $L = s(1)$ is the overall curve length. If the non-overlapping condition:

$$|\rho| R < 1 \qquad (16)$$

is not fulfilled, the center of the osculating circle of $\mathcal{C}$ of radius $1/|\rho|$ is inside the virtual image G, thus some points in the vicinity of this center are defined at least twice. However, in a practical point of view, experience shows that it is possible to overcome this second condition as soon as the sharp corners of $\mathcal{C}$ do not exceed the right angle because sharper angles put in coincidence inner black points of G with outer white points of F. At last, from Eq. (13) the curve must not have any stationary points:

$$\left\| \frac{\partial \mathbf{X}^c}{\partial x_1} \right\| > 0 \qquad (17)$$

## 3 Uncertainty of the VIC measurement

3.1 Set of simplified equations in ideal cases

In order to study the precision of the method, the above set of equation is simplified hereafter. At first we suppose that, close to the solution, $F(\mathbf{X}) \simeq f(x_2)$ (as it is the case for $g$, see Eqs. (1, 2)) thus:

$$\frac{\partial F}{\partial \mathbf{X}} = \frac{f'}{R} \mathbf{e}_r \qquad (18)$$

Together with Eq. (13), this allows the separation of variables in Eq. (10):

$$\frac{\partial \psi}{\partial \lambda_p} = \frac{1}{R} \int_{0}^{1} \frac{\partial \mathbf{X}^c}{\partial \lambda_p} \cdot \mathbf{e}_r \, dx_1 \int_{-1}^{1} f'(f - g) dx_2 \qquad (19)$$

The current term of the first integral is null if $\partial \mathbf{X}^c / \partial \lambda_p$ is everywhere collinear to $\mathbf{e}_s$, corresponding to a tangential motion which lets the curve unchanged: such case has to be avoided when choosing a curve equation. Thus, at convergence of the Newton scheme, when $\partial \psi / \partial \lambda_p = 0$:

$$\int_{-1}^{1} f'(f - g) dx_2 = 0 \tag{20}$$

At last, if the virtual image borders lie one in the white background and one in the black silhouette: $f(-1) = 0$ and $f(1) = 1$, an integration by parts gives:

$$\frac{1}{2} \int_{-1}^{1} \left( f(x_2) - \frac{1}{2} \right) dx_2 = 0 \tag{21}$$

which shows that, at convergence, the mean value of $f$ is $1/2$.
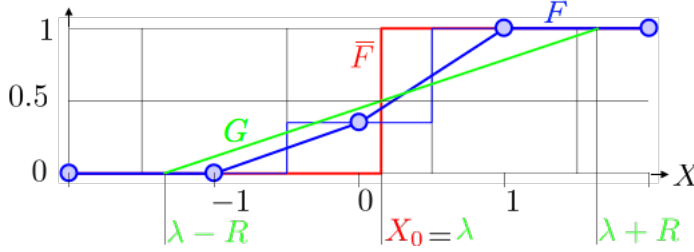
3.2 Exact 1D discrete measurement



**Fig. 3** 1D VIC. Luminance $\bar{F}$ (red), digital image and its linear interpolation $F$ (blue), virtual image $G$ at best correlation (green)

Let $\bar{F}(X) = H(X - X_0)$, where $H$ is the Heavyside distribution, be the physical luminance of a 1D silhouette (Fig. 3). Supposing ideal sensor (linear and homogenous) and optics, the $i^{\text{th}}$ pixel returns the value $\int_{i-1/2}^{i+1/2} \bar{F} dX$ (blue dots). In 1D, the curve $\mathcal{C}$ is degenerated into a point ($x_1$ is meaningless) whose parameterized equation is simply chosen as $X^c = \lambda$ and the mapping (Eq. 3) reduces to $X = \lambda + Rx_2$. Due to the absence of curvature, expressions $\Psi$ (Eq. 6) and $\psi$ (Eq. 7) are equivalent thus Eq. (21) corresponds to:

$$\frac{1}{2R} \int_{\lambda-R}^{\lambda+R} \left( F(X) - \frac{1}{2} \right) dX = 0, \tag{22}$$

if $f(-1) = F(\lambda - R) = 0$ and $f(1) = F(\lambda + R) = 1$, *i.e.* if the support of $G$ is wide enough: $\lambda - R < -1$ and $\lambda + R > 1$. Because $-0.5 < \lambda < 0.5$, this leads to impose $R > 1.5$. Solving this integral with the analytical expression $F(X)$ of

the linear interpolation (thick blue segments in Fig. 3) gives straightforwardly $\lambda = X_0$. This shows that the VIC measurement $X^c$ corresponds exactly to the prescribed edge location $X_0$, whatever $X_0$ and $R > 1.5$.

### 3.3 Uncertainty due to curve mismatch and local correlation indicator

The VIC method requires the user-chosen curve $\mathcal{C}$ to be able to fit the contour of interest. Fig. 4 shows that, if the curve matches, f appears as invariant along $x_1$ (very similar to g) but shows waviness in the opposite case. However, a more objective indicator is necessary to quantify the quality of the identification. A straightforward idea consists in using $\partial\psi/\partial x_1$ as local correlation function but, g being not physical and $R$ being user chosen, this function only brings a qualitative information and does dot distinguish if the curve is inside or outside the contour.
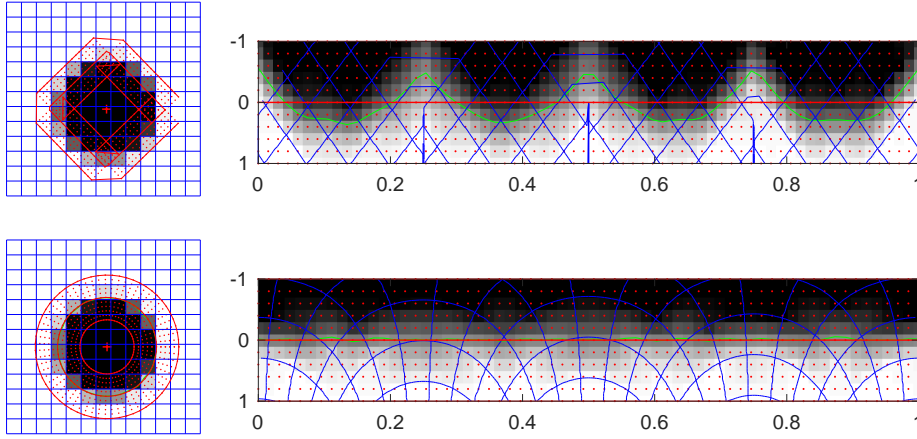


**Fig. 4** Images F (left) and f (right) of a small disc identified by a square (top) and a circle (bottom). Pixel edges (blue), computational points (red) and correlation indicator $\mu$ (green)

From Eq. (21), we define the signed distance:

$$\mu(x_1) = \int_{-1}^{1} \left( \frac{1}{2} - f(x_1, x_2) \right) dx_2 \tag{23}$$

This one is defined in the frame $\mathbf{x}$ and corresponds to $\mu R$ in the pixel frame $\mathbf{X}$. Fig. 4 shows that $\mu(x_1)$ represents a local identification of the boundary.

Fig. 5 is related to the well-know impossibility for a B-Spline to depict a circle [11]. When using a 10 points B-Spline, a peak of magnitude $\simeq 0.05$ pixel at wavelength 63 pixels ($\simeq L/10$ pixel) is visible in the FFT of $R\mu$. It reveals a periodic oscillation of the curve from inside to outside of the exact circle
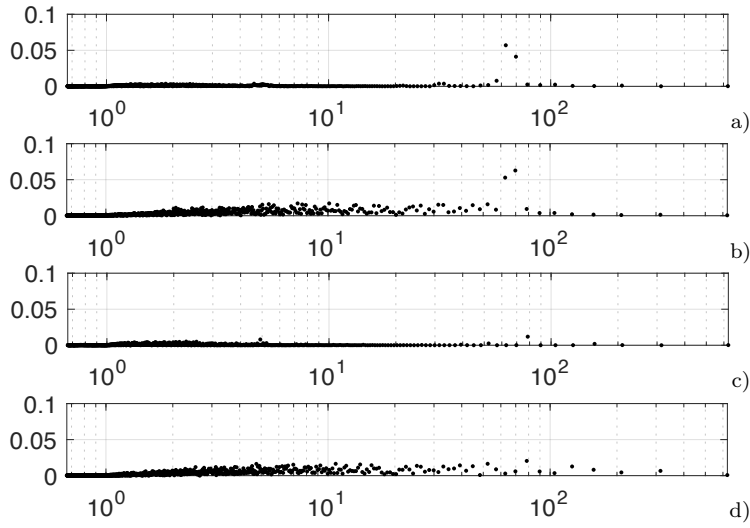
**Fig. 5** FFT of $R\mu$ for a 100 pixel radius disc with (a) $\sigma_0 = 0$ and 10 points B-Spline, (b) $\sigma_0 = 0.1$ and 10 points B-Spline, (c) $\sigma_0 = 0$ and circle, (d) $\sigma_0 = 0.1$ and circle.

in between the ten (regularly spaced) control points, which would be hard to see on a representation such has Fig. 4. Cases with noisy images lead to an additional noise spectrum whose mean amplitude is close to the estimation of Eq. (32) of $21 \times 10^{-3}$ for the B-Spline and $8 \times 10^{-3}$ for the circle.

Curve mismatching induces long wave oscillations of $R\mu$ which are revealed by a spectral analysis as long as they are not hidden by image noise. The acceptable precision, *i.e.* the magnitude of the maximum peak, remains the the user's decision.

3.4 Uncertainty associated to discretization

If the VIC has been shown in Sec. 3.2 to be theoretically exact in 1D, things are more complicated in 2D. The pixel grid is used as computational frame in most of image analysis methods, including DIC and some versions of VIC using $\Psi$ [13]. However, many tests showed that computing on a regular discretization of $(x_1, x_2)$ (see Fig. 4) provides better precision, as soon as the distance between two corresponding points $(X_1, X_2)$ is less than 1/3 pixel [15].

The values of F, required for Eq. (7) at these non integer values are obtained by interpolation. Another series of tests showed that the simplest and fastest linear interpolation gives equivalent or even better precision than cubic or B-spline interpolation. This is different from DIC, but in accordance with the analytical analysis in Sec. 3.2.

**Fig. 6** Line segment test with small angle of inclination

In Sec. 3.2 we showed that $R$ should be greater than 1.5 pixel. In order to set the optimal value of $R$ for 2D images, we proceed to tests on synthetic images of linear edges identified with a line segment (Fig. 6). To address any cases, the angle $\theta$ from $X_1$ to the edge is varied from 0 to $\pi/4$, the ordinate of its midpoint is varied of $\Delta X_{02} \in [0, 1[$ pixel and the length $L = 100$ of the segment is varied of $\Delta L \in [0, 1[$ pixel. Ten levels are used for each variation. The mean $m_d$ and the standard deviation $\sigma_d$ of the distance $\delta(x_1)$ between identified and exact segments are computed. In average, setting $R = 1.5$ gives $m_d = -4.09 \times 10^{-5}$ and $\sigma_d = 3.76 \times 10^{-4}$ and setting $R = 2$ gives $m_d = -5.99 \times 10^{-5}$, $\sigma_d = 7.92 \times 10^{-4}$.

However Fig. 7 shows that choosing $R = 2$ eliminates pathologic cases of small angles (such as shown by Fig. 6). Setting other (especially larger) values for $R$ did not provide any advantage. As a consequence, $R = 2$ appears to be the optimal value for the VIC.
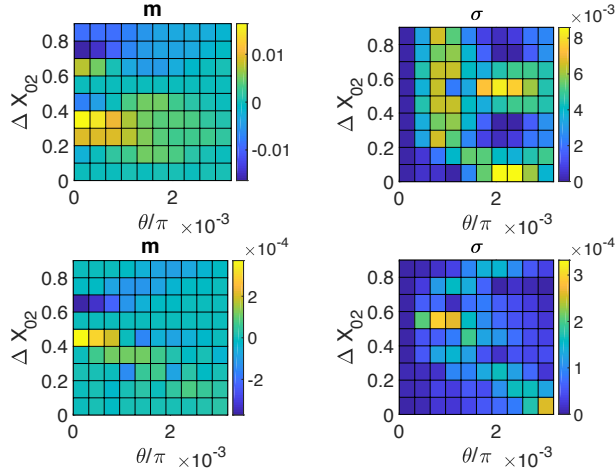


**Fig. 7** Statistics on the line segment test at small angles for $R = 1.5$ (top) and $R = 2$ (bottom)

In order to get an estimator of the uncertainty associated to the sole effect of discretization, similar line segment tests have been realized, varying the length $L$ over two decades. Fig. 8 shows that the mean distance $m_d$ is weak for all $L$ and that the standard deviation $\sigma_d$ is very close to its linear regression
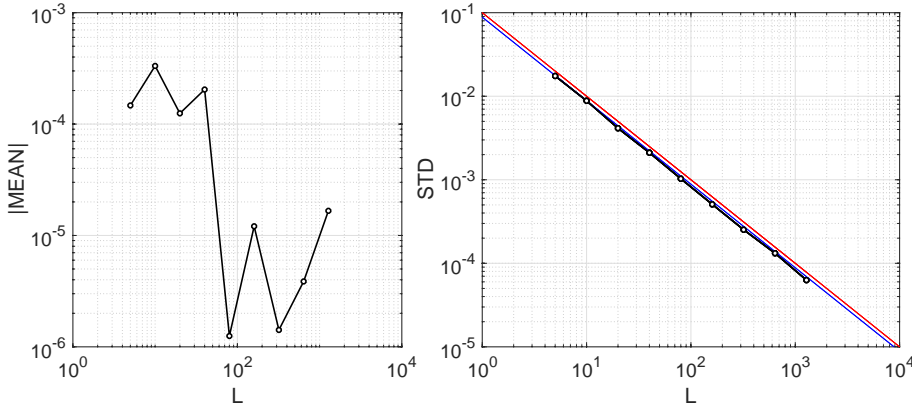
**Fig. 8** Statistics of the line segment test with variable length

$\sigma_d = 0.0885/L$ (blue line on Fig. 8). The proposed empirical rule:

$$\sigma_d \simeq \frac{N}{20L} \tag{24}$$

corresponds to the red line. The role of the number of curve parameters $N$ in this equation, of two in these tests (ordinate and angle), is supposed to be equivalent to the one it has in Eq. (32).

3.5 Uncertainty associated to brightness and contrast defects

At ideal, the silhouette is black and the background is white. However, real images may have contrast and luminance deviations. From Sec. 3.2, the average of $F(X)$ over all possible $X_0 \in [-0.5, 0.5]$ is linear: $< F >= (X + 1)/2$. Thus, for this analytical study, we suppose $f$ to be the continuous linear piecewise function (see Fig. 9):

$$x_2 < \frac{\delta - 1}{R} \implies f(x_2) = b + \frac{1 - a}{2}$$
$$\frac{\delta - 1}{R} \le x_2 < \frac{\delta + 1}{R} \implies f(x_2) = a\frac{Rx_2 - \delta}{2} + b + \frac{1}{2}$$
$$\frac{\delta + 1}{R} \le x_2 \implies f(x_2) = b + \frac{1 + a}{2} \tag{25}$$

where $a$ is the amplitude (contrast), $b$ the bias (luminance), $\delta/R$ the location of the researched edge. The origin of the virtual image at $x_2 = 0$ defines the VIC measurement thus $\delta/R$ (in the frame $\mathbf{x}$) or $\delta$ (in the pixel frame $\mathbf{X}$) is the measurement error. Used together with Eq. (20), which is fulfilled at convergence, above expressions give:
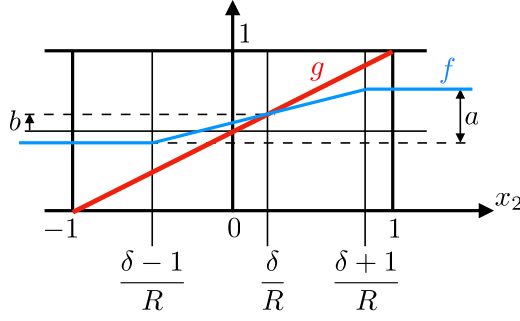
$$\delta = 2Rb \tag{26}$$

**Fig. 9** Study of amplitude $a$ and bias $b$ effects

As a consequence, the contrast $a$ has no influence on the precision but a luminance variation $b$ induces a bias $\delta$ in the measurement. In a practical point of view, this is easily annulated during computation by a linear correction of the gray levels of F. Similar calculus shows that non linear image corrections should be avoided because they induce a bias. In particular, best results will be obtained with CCD sensors with good linearity.

3.6 Uncertainty associated to image noise

Inevitable image noise leads to uncertainty in the VIC measurement. We suppose now that each pixel of integer coordinates $(i, j)$ is the sum of an exact value $F_{ij}$ and a gaussian noise $N_{ij}$, spatially uncorrelated, of zero mean and of standard deviation $\sigma(N_{ij}) = \sigma_0$. With the hypothesis of Sec. 3.1, we show in Annex B that:

$$\sigma\left(\frac{\partial\psi}{\partial\lambda_p}\right) \simeq \frac{\sigma_0}{R\sqrt{2RL}}\sqrt{\int_0^1 \left(\frac{\partial\mathbf{X}^c}{\partial\lambda_p}\cdot\mathbf{e}_r\right)^2 dx_1} \qquad (27)$$

From the Newton scheme (Eq. 8), this term is associated to the standard deviation of each shape parameter by:

$$\sigma^2\left(\frac{\partial\psi}{\partial\lambda_p}\right) = \left(\frac{\partial^2\psi}{\partial\lambda_p\partial\lambda_q}\right)^2 \sigma^2(\lambda_q) \qquad (28)$$

The average $\sigma_n$ of the standard deviation of the distance $\mathbf{X}^c\cdot\mathbf{e}_r$ from the measurement to the noiseless solution is:

$$\sigma_n^2 = \int_0^1 \sigma^2\left(\mathbf{X}^c\cdot\mathbf{e}_r\right) dx_1 \qquad (29)$$

From $d\mathbf{X}^c = (\partial\mathbf{X}^c/\partial\lambda_q)\,d\lambda_q$ we deduce:

$$\sigma^2\left(\mathbf{X}^c\cdot\mathbf{e}_r\right) = \sum_q \left(\frac{\partial\mathbf{X}^c}{\partial\lambda_q}\cdot\mathbf{e}_r\right)^2 \sigma^2(\lambda_q) \qquad (30)$$

Gathering previous expressions gives $\sigma_n^2$. However this complex expression has to be computed in each cases. A simpler approximation is obtained by supposing at first a perfectly contrasted image with $a = 1$ and $b = 0$. Eq. (25) and Eq. (12) give:

$$\frac{\partial^2 \psi}{\partial \lambda_p \partial \lambda_q} = \frac{1}{2R} \int_0^1 \left( \frac{\partial \mathbf{X}^c}{\partial \lambda_p} \cdot \mathbf{e}_r \right) \left( \frac{\partial \mathbf{X}^c}{\partial \lambda_q} \cdot \mathbf{e}_r \right) dx_1 \qquad (31)$$

At second we retain only the diagonal terms of this matrix, which corresponds to consider that each shape variable acts on a separate part of the curve. This gives a simple approximation of the VIC standard deviation due to the image noise:

$$\sigma_n = \sigma_0 \sqrt{\frac{2N}{RL}} \qquad (32)$$

The proportionality between $\sigma_n$ and the image noise $\sigma_0$ is common with DIC uncertainty analysis [14,19,18,3]. Doubling the image resolution doubles $L$ thus divides $\sigma_n$ by $\sqrt{2}$. The uncertainty $\sigma_n$ is proportional to $\sqrt{N}$: this weak dependance allows the user to retain complex curve families. This formula erroneously suggest the use of large $R$ but the calculus is valid for the active part of the virtual image thus one may consider $R \leq 2$. The quantification noise, of classical expression $\sigma_{0q} = (2^{nb}\sqrt{12})^{-1}$ where $nb$ is the bit depth, can also be taken into account as an additional image noise.
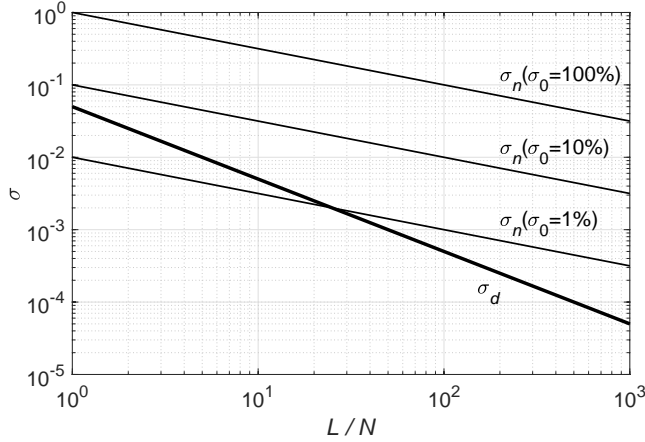
3.7 Summary



**Fig. 10** Uncertainty of the VIC method, for $R = 2$

Fig. 10 shows the uncertainty of the method, according to expressions of $\sigma_d$ (Eq. 24) and $\sigma_n$ (Eq. 32). It shows in particular that the irreducible uncertainty $\sigma_d$, associated to discretization, can only be attained with low image

noise $\sigma_0$ and large curve support $L/N$. Of course this graph is valid only in absence of curve fitting error.

## 4 Validation and comparison of the VIC uncertainty

### 4.1 Validation of the proposed expressions

In table 1 we compare predicted and measured uncertainties on various tests. Cases $C_1$ to $C_4$ correspond to numerical tests onto a $401 \times 401$ pixels image of a spiral [15]. Cases $D_1$ to $D_3$ refer to synthetic images of discs of average radii respectively of 3 (Fig. 4), 10, 100 pixels whose center and radius are randomly varied over 1 pixel, over 100 trials. Cases $D_1'$ to $D_3'$ are similar, but with an additive gaussian image noise $\sigma_0$. All images are in 8 bits. The standard deviation associated to discretization $\sigma_d$ is obtain by Eq. (24) and the one associated to image noise $\sigma_n$ by Eq. (32). The quantification noise $\sigma_{0q}$ is took into account in $\sigma_n$. One observes that the predicted values of $\max(\sigma_d, \sigma_n)$ are

**Table 1** Predicted ($\sigma_d$, $\sigma_n$) and measured ($\sigma$) standard deviations. Mesured mean ($m$)

| case | $R$ | $L$ | $N$ | $\sigma_0$ | $\sigma_d \times 10^3$ | $\sigma_n \times 10^3$ | $\sigma \times 10^3$ | $m \times 10^3$ |
|------|-----|-----|-----|-----------|------------------------|------------------------|----------------------|-----------------|
| $C_1$ | 1 | 1236 | 20 | 0% | 0.809 | 0.20 | 9 | |
| $C_2$ | 1 | 1236 | 20 | 30% | 0.809 | 54.2 | 54 | |
| $C_3$ | 1 | 1236 | 20 | 50% | 0.809 | 90.1 | 85 | |
| $C_4$ | 1 | 1236 | 20 | 90% | 0.809 | 163 | 180 | |
| $D_1$ | 2 | 18.8 | 3 | 0% | 7.96 | 8.41 | 4 | $-1.71$ |
| $D_1'$ | 2 | 18.8 | 3 | 10% | 7.96 | 48.3 | 56 | 2.12 |
| $D_2$ | 2 | 62.8 | 3 | 0% | 2.39 | 2.63 | 0.96 | $-0.21$ |
| $D_2'$ | 2 | 62.8 | 3 | 10% | 2.39 | 24.5 | 30 | 0.26 |
| $D_3$ | 2 | 628 | 3 | 0% | 0.24 | 0.32 | 0.24 | 0.00 |
| $D_3'$ | 2 | 628 | 3 | 10% | 0.24 | 7.23 | 8 | 0.86 |

in good agreement with measured ones $\sigma$. The sole exception is the case $C_1$ for which a curve fitting error is present, the 10 control points of the B-Spline being not enough to describe the spiral at this level of precision.

### 4.2 Comparison between the VIC and other methods uncertainties

The VIC method has been already successfully compared to Fast Marching Algorithm [16] and Steger's method [17] in earlier publication [15]. Since this article, new methods also claimed for sub-pixel precision. Among them we retained the work of Trujilo-Pino (TP) [21,20] which, based on an area estimate, is in some way close to the estimator $\mu$ (Eq. 29). For reference, we retained the well known Active Contours (AC) method [10]. Table 2 shows the results obtained for the circular disc statistical study. With respect to TP

**Table 2** Measured uncertainty for active contours (AC) and Trujilo-Pino's (TP) methods

| case | AC | | TP | |
|---|---|---|---|---|
| | $\sigma \times 10^3$ | $m \times 10^3$ | $\sigma \times 10^3$ | $m \times 10^3$ |
| $D_1$ | 44 | $-93$ | 6 | 3.94 |
| $D_1'$ | 75 | $-110$ | 227 | 7.08 |
| $D_2$ | 30 | $-31$ | 2.04 | $-0.12$ |
| $D_2'$ | 71 | $-35$ | 231 | $-2.18$ |
| $D_3$ | 27 | $-4.52$ | 1.95 | 0.01 |
| $D_3'$ | 69 | $-4.59$ | 236 | 1.55 |

method, the VIC (table 1) offers a gain in $\sigma$ which increases with $L/N$. In the realistic case $D_3$, with $L/N \simeq 200$ pixels per curve parameter, the VIC is approximatively 6 times more precise than the TP method. The AC method gives worse results but still identifies a continuous contour in noisy images, on the contrary of TP method which required to remove aberrants points (farther than 0.5 pixel). Both TP and AC methods, like the majority of the existing contour detection methods, are local ones. On the contrary, the VIC benefits of the regularization associated to the curve $\mathcal{C}$, whose effect on the precision, from Eqs. (24, 32), increases with the curve length.

## 5 Conclusions

With a reliable expression of the uncertainty and a tool to estimate the relevance of the chosen curve family, the Virtual Image Correlation method has now reached maturity. This article gives it a clarified theoretical framework and the sole parameter of the method, the virtual image width, is now fixed.

Relative interests between local and global methods are subjects of endless debates in the DIC community [22]. As expected, the VIC has the same advantages as the global DIC: accuracy and robustness to noise, but also shares its disadvantages: the necessity to choose an *a priori* field (DIC) or curve (VIC). Furthermore the given measure does not consist in a set of pixels but in a continuous curve defined from a reduced set of shape parameters. The initialization step required for the VIC can be helped by temporarily setting a wide virtual image width $R$ or by using one of the many existing detection method, for example the robust Active Contours method. Remaining possible ameliorations of the VIC may consist in faster computational strategies and some work remain to be done in 3D.

The field of applications is wide, especially in experimental mechanics. The VIC can be used to measure object boundaries [5,9], the shape of elongated objects (beam, trusses...) [2] and possibly compare these curves between free and strained states. The line of interest can also be a 2D [4] or 3D [13] crack or a physical front (chemical, thermal, hydric...) [6]. Recent developments

concern the use of the VIC to improve the DIC's precision close to the object borders [1].

## A Relative magnitude of major terms

The relative magnitude of the terms in Eq. (11) are compared together in order to justify the use of the simplified Eq. (12). We suppose that, close to solution, $F(\mathbf{X}) \simeq f(x_2)$. If $\rho \ll R$, Eq. (18) can be expressed as:

$$\frac{\partial^2 F}{\partial \mathbf{X}^2} \simeq \frac{f''(x_2)}{R^2} \mathbf{e}_r \otimes \mathbf{e}_r \tag{33}$$

where $\otimes$ denotes the dyadic (tensor) product. Then, the terms of interest in Eqs. (10, 11) can be rewritten in a separate form:

$$I_2 = \int_{-1}^{1} \int_{0}^{1} \left( \frac{\partial \mathbf{X}}{\partial \lambda_p} \cdot \frac{\partial^2 F}{\partial \mathbf{X}^2} \cdot \frac{\partial \mathbf{X}}{\partial \lambda_q} \right) (f - g) dx_1 dx_2$$

$$\simeq \frac{1}{R^2} \int_{0}^{1} \left( \frac{\partial \mathbf{X}^c}{\partial \lambda_p} \cdot \mathbf{e}_r \right) \left( \frac{\partial \mathbf{X}^c}{\partial \lambda_q} \cdot \mathbf{e}_r \right) dx_1 \quad \int_{-1}^{1} f''(f - g) dx_2 \tag{34}$$

$$I_3 = \int_{-1}^{1} \int_{0}^{1} \left( \frac{\partial F}{\partial \mathbf{X}} \cdot \frac{\partial^2 \mathbf{X}}{\partial \lambda_p \partial \lambda_q} \right) (f - g) dx_1 dx_2$$

$$\simeq \int_{0}^{1} \left( \frac{\partial^2 \mathbf{X}^c}{\partial \lambda_p \partial x_1} \cdot \mathbf{e}_r \right) \left( \frac{\partial^2 \mathbf{X}^c}{\partial \lambda_q \partial x_1} \cdot \mathbf{e}_r \right) dx_1 \quad \int_{-1}^{1} x_2 f'(f - g) dx_2 \tag{35}$$

$$I_4 = \int_{-1}^{1} \int_{0}^{1} \left( \frac{\partial F}{\partial \mathbf{X}} \cdot \frac{\partial \mathbf{X}}{\partial \lambda_p} \right) \left( \frac{\partial F}{\partial \mathbf{X}} \cdot \frac{\partial \mathbf{X}}{\partial \lambda_q} \right) dx_1 dx_2$$

$$= \frac{1}{R^2} \int_{0}^{1} \left( \frac{\partial \mathbf{X}^c}{\partial \lambda_p} \cdot \mathbf{e}_r \right) \left( \frac{\partial \mathbf{X}^c}{\partial \lambda_q} \cdot \mathbf{e}_r \right) dx_1 \quad \int_{-1}^{1} (f')^2 dx_2 \tag{36}$$

Integrals over $x_2$ ($i_2, i_3, i_4$), in correspondance with ($I_2, I_3, I_4$), depend upon $g(x_2)$ (Eq. 2)
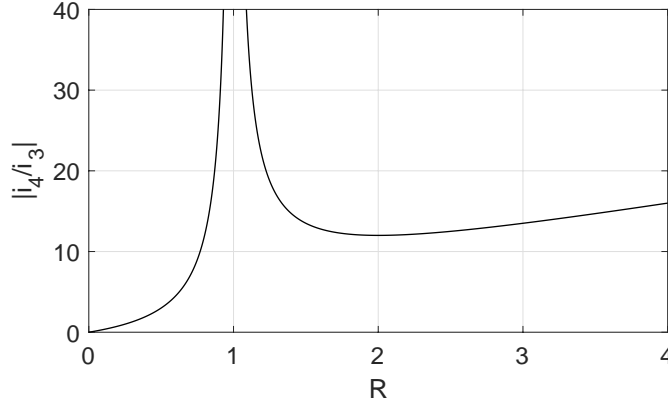


**Fig. 11** Ratio $|i_4/i_3|$

and $f(x_2)$. According to Eq. (25), in an ideal case $a = 1$, $b = 0$ and $\delta = 0$, $f(x_2) = (1 + Rx_2)/2$ thus: $i_2 = 0$, $i_3 = (R - 1)/6R^2$ if $R > 1$ or $i_3 = R(R - 1)/6$ if $R < 1$ and $i_4 = 1/2$ if $R > 1$ or $i_4 = R^2/2$ else. Fig. 11 shows that $i_3 \ll i_4$ as soon as $R > 1$, *i.e* as soon as the virtual image width is wide enough to cover the black to white transition in F. This result justifies the simplification from Eqs. (11, 12), as soon as the integrals over $x_1$ have comparable magnitudes.

## B Intermediate calculations on the effect of image noise

Hypotheses of Sec. 3.1, Eqs. (19) and (21) lead to:

$$\frac{\partial \psi}{\partial \lambda_p} = \frac{1}{2R} \int_0^1 \int_{-1}^1 \frac{\partial \mathbf{X}^c}{\partial \lambda_p} \cdot \mathbf{e}_r \left( f(x_2) - \frac{1}{2} \right) dx_1 dx_2 = 0 \tag{37}$$

Eqs. (3 to 15) give the differential surface element in the frame $\mathbf{X}$:

$$d\mathbf{X} = \left( \frac{\partial \mathbf{X}^c}{\partial x_1} + \rho R x_2 \left\| \frac{\partial \mathbf{X}^c}{\partial x_1} \right\| \mathbf{e}_s \right) dx_1 + R dx_2 \, \mathbf{e}_r \tag{38}$$

Supposing a weak curvature $|\rho| R \ll 1$ we obtain:

$$dX_1 dX_2 \simeq RL dx_1 dx_2 \tag{39}$$

which gives the correspondance between the virtual image surfaces $S = 2RL$ in the frame $\mathbf{X}$ and $s = 2$ in the frame $\mathbf{x}$. In the pixel frame, Eq. (37) corresponds to:

$$\frac{\partial \psi}{\partial \lambda_p} \simeq \frac{1}{Rn} \sum_{ij} \left( \frac{\partial \mathbf{X}^c}{\partial \lambda_p} \cdot \mathbf{e}_r \right)_{ij} \left( F_{ij} + N_{ij} - \frac{1}{2} \right) \tag{40}$$

where $n$ is the number of pixels involved in the virtual image calculus thus $n \simeq 2RL$ (the virtual image surface). From elementary statistics, we obtain the standard deviation:

$$\sigma \left( \frac{\partial \psi}{\partial \lambda_p} \right) \simeq \frac{\sigma_0}{2LR^2} \sqrt{\sum_{ij} \left( \frac{\partial \mathbf{X}^c}{\partial \lambda_p} \cdot \mathbf{e}_r \right)_{ij}^2} \tag{41}$$

and Eq. (27) is deduced from this equation and the following correspondance between continuous and discrete expressions:

$$\sum_{ij} \left( \frac{\partial \mathbf{X}^c}{\partial \lambda_p} \right)^2 \simeq 2RL \int_0^1 \left( \frac{\partial \mathbf{X}^c}{\partial \lambda_p} \right)^2 dx_1, \tag{42}$$

## References

1. Baconnais, M., Réthoré, J., François, M.: Improvement of the digital image correlation close to the object borders. Strain (proposed)
2. Bloch, A.: Expérimentation et modélisation du comportement des structures gonflables complexes sous chargement climatique aléatoire. Ph.D. thesis, Université de Nantes (2015)
3. Bornert, M., Doumalin, P., Dupré, J.C., Poilâne, C., Robert, L., Toussaint, E., Wattrisse, B.: Assessment of digital image correlation measurement accuracy in the ultimate error regime: Improved models of systematic and random errors. Experimental Mechanics **58**(1), 33–48 (2018). DOI 10.1007/s11340-017-0328-5
4. François, M.L.M.: Monitoring of debonding or cracking in bending tests by virtual image correlation. In: A. Chabot, W. Buttlar, E. Dave, C. Petit, G. Tebaldi (eds.) 8th RILEM Int. Conf. on Mechanisms on Cracking and Debonding in Pavements (MCD2016), Nantes, pp. 739–748. Springer (2016)
5. François, M.L.M., Bloch, A., Thomas, J.C.: Metrology of contours by the virtual image correlation technique. In: SEM (ed.) Advancement of Optical Methods in Experimental Mechanics, volume 3, SEM 2015 Annual Conference and Exposition on Experimental and Applied Mechanics,, pp. 239–246. SEM, Springer, Costa-Mesa, USA (2015)

6. François, M.L.M., Semin, B., Auradou, H.: Identification of the shape of curvilinear beams and fibers. Applied Mechanics and Materials **24-25**, 359–364 (2010)

7. Hild, F., Roux, S.: Digital image correlation: from displacement measurement to identification of elastic properties - a review. Strain **42**(2), 69–80 (2006)

8. Hild, F., Roux, S.: Measuring stress intensity factors with a camera: integrated digital image correlation (I-DIC). Comptes Rendus de Mécanique **334**, 8–12 (2006)

9. Jiang, Z., Witz, J.F., Lecomte-Grosbras, P., Dequidt, J., Duriez, C., Cosson, M., Cotin, S., Brieu, M.: B-spline based multi-organ detection in magnetic resonance imaging. Strain **51**, 235–247 (2015)

10. Lankton, S.: Active contour segmentation. https://fr.mathworks.com/matlabcentral/fileexchange/19567-active-contour-segmentation (Retrieved July 9, 2019). MATLAB Central File Exchange

11. Piegl, L., Tiller, W.: A menagerie of rational B-spline circles. IEEE Computer Graphics and Applications **9**(5), 48–56 (1989)

12. Réthoré, J., François, M.L.M.: Corrélation d'images pour la détection de contour. In: Actes du 20e Congrès Français de Mécanique. Besançon (2011)

13. Réthoré, J., François, M.L.M.: Curve and boundaries measurement using B-splines and virtual images. Optics and Lasers in Engineering **52**, 145–155 (2013)

14. Roux, S., Hild, F.: Stress intensity factor measurements from digital image correlation: post-processing and integrated approaches. International Journal of Fracture **140**, 141–157 (2006)

15. Semin, B., Auradou, H., François, M.L.M.: Accurate measurement of curvilinear shapes by virtual image correlation. The European physical journal applied physics **56**, 1–10 (2011)

16. Sethian, J.: Level Set Methods and Fast Marching Methods. Cambridge University Press (1998)

17. Steger, C.: An unbiased detector of curvilinear structures. IEEE Transactions on Pattern Analysis and Machine Intelligence **20**(2), 113–125 (1998)

18. Su, Y., Zhang, Q., Xu, X., Gao, Z.: Quality assessment of speckle patterns for DIC by consideration of both systematic errors and random errors. Optics and Lasers in Engineering **86**, 132–142 (2016). DOI 10.1016/j.optlaseng.2016.05.019

19. Sutton, M.A., Orteu, J.J., Schreier, H.W.: Image Correlation for Shape, Motion and Deformation Measurements. Basic Concepts, Theory and Applications. Springer (2009). DOI 10.1007/978-0-387-78747-3

20. Trujillo-Pino, A.: Accurate subpixel edge location. https://www.mathworks.com/matlabcentral/fileexchange/48908-accurate-subpixel-edge-location (Retrieved June 28, 2019). MATLAB Central File Exchange

21. Trujillo-Pino, A., Krissian, K., Alemán-Flores, M., Santana-Cedrés, D.: Accurate subpixel edge location based on partial area effect. Image and Vision Computing **31**, 72–90 (2013)

22. Wang, B., Pan, B.: Subset-based local vs. finite element-based global digital image correlation: A comparison study. Theoretical and Applied Mechanics Letters **6**(5), 200–208 (2016). DOI https://doi.org/10.1016/j.taml.2016.08.003. URL http://www.sciencedirect.com/science/article/pii/S2095034916300411